Uncovering Thermal and Electrical Properties of Sb$_2$Te$_3$/GeTe Superlattice Films

Heungdong Kwon, Asir Intisar Khan, Christopher Perez, Mehdi Asheghi, Eric Pop, and Kenneth E. Goodson*
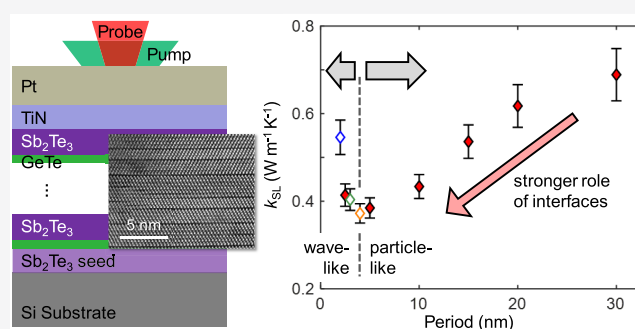
ACCESS | Metrics & More | Article Recommendations | Supporting Information

ABSTRACT: Superlattice-like phase change memory (SL-PCM) promises lower switching current than conventional PCM based on Ge$_2$Sb$_2$Te$_5$ (GST); however, a fundamental understanding of SL-PCM requires detailed characterization of the interfaces within such an SL. Here we explore the electrical and thermal transport of SLs with deposited Sb$_2$Te$_3$ and GeTe alternating layers of various thicknesses. We find up to an approximately four-fold reduction of the effective cross-plane thermal conductivity of the SL stack (as-deposited polycrystalline) compared with polycrystalline GST (as-deposited amorphous and later annealed) due to the thermal interface resistances within the SL. Thermal measurements with varying periods of our SLs show a signature of phonon coherence with a transition from wave-like to particle-like phonon transport, further described by our modeling. Electrical resistivity measurements of such SLs reveal strong anisotropy (~2000×) between the in-plane and cross-plane directions due to the weakly interacting van der Waals-like gaps. This work uncovers electrothermal transport in SLs based on Sb$_2$Te$_3$ and GeTe for the improved design of low-power PCM.

KEYWORDS: *Sb$_2$Te$_3$/GeTe superlattice, time-domain thermoreflectance, thermal conductivity, electrical resistivity, anisotropy*

In recent years, there has been a large and growing interest in new materials for new data storage opportunities. These opportunities are driven in equal parts by the growing memory demands of artificial intelligence applications and by the shortcomings of existing memory technologies such as flash (nonvolatile, but relatively slow) and DRAM (fast, but volatile).[1,2] In this context, phase change memory (PCM) has become a key emerging technology,[3] with Intel and Micron jointly introducing a commercial PCM-based product called 3D X-point in 2017. However, PCM improvements remain necessary, including reduced resistance drift, higher endurance, and lower switching current density, ideally <1 MA cm^{-2}.[1,3]

Several recent studies have suggested that replacing the phase-change material (conventionally Ge$_2$Sb$_2$Te$_5$, i.e., GST) with a superlattice (SL) of alternating thin chalcogenide films (e.g., Sb$_2$Te$_3$ and GeTe) could offer lower switching power, faster switching speed, and higher endurance.[4,5] Interestingly, the fundamental operation of SL-PCM is not well understood. It was initially proposed that its memory states are controlled at the internal interfaces by subtle changes in the position of Ge atoms in multilayered Sb$_2$Te$_3$/GeTe films.[6] However, the broader influence of internal interfaces on electrical and thermal transport in SL-PCM remains poorly understood, especially when considering that conventional PCM is driven by a thermally induced phase-change mechanism. In addition,

the complex physics of energy and charge transport at these interfaces also presents an opportunity to better understand the mechanism of SL-PCM device switching.
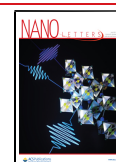
In the past, both our groups and others have demonstrated the benefits of thermal engineering of PCMs (e.g., by increasing their thermal resistance) by introducing multilayer dielectric insulation,[7−9] graphene,[10] MoS$_2$,[11] and other interface layers[12,13] to reduce the switching current and power density. The influence of PCM interfaces and of ballistic heat flow[14] are only expected to become magnified in ultrathin nanoscale films and devices and, in particular, in SL structures that have numerous *internal* interfaces.[15] In fact, recent results suggest that the low switching current in SL-PCM could be thermally driven due to the thermal resistance of interfaces within the PCM stack.[14,16]

Motivated by the need for a deeper understanding of SL-PCM materials, here we report the thermal and electrical transport characterization of Sb$_2$Te$_3$/GeTe SLs by measuring
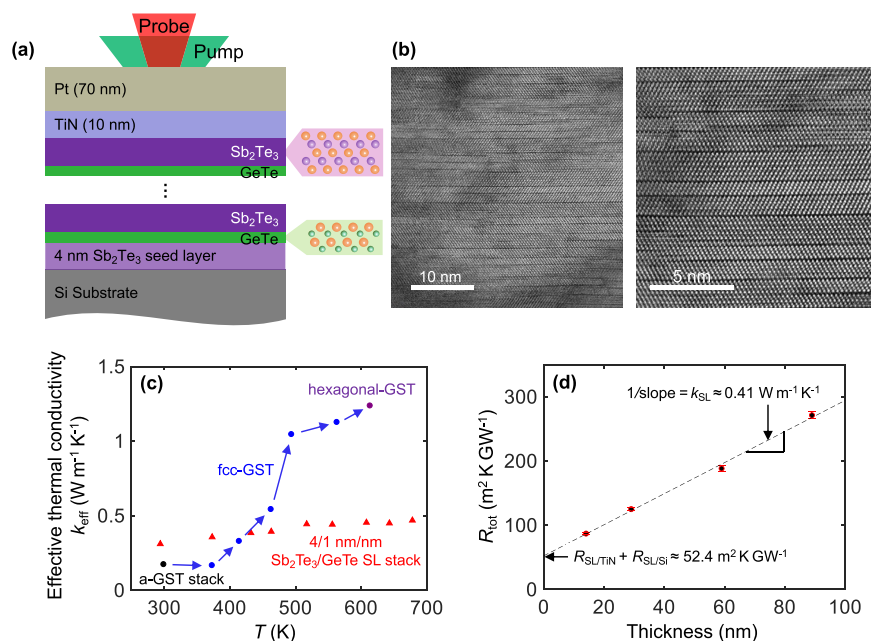
Figure 1. Cross-plane thermal characterization of Sb_2Te_3/GeTe superlattices (SLs). (a) Measurement setup showing, from bottom to top: silicon (Si) substrate, 4 nm Sb_2Te_3 seed layer, deposited alternating GeTe and Sb_2Te_3 layers, TiN/Pt capping layers, and pump/probe lasers. (b) High-resolution scanning transmission electron microscopy (STEM) cross-sections of the resulting superlattice on a 100 mm diameter Si wafer, revealing sharp interfaces and clear van der Waals-like gaps. The resulting superlattice is somewhat different from the as-deposited layers due to interfacial reconstruction, which is known to occur during deposition kinetics.[18−20] (c) Measured effective thermal conductivity of the 60 nm thick as-deposited SL including the TiN capping layer (red solid triangles) from room temperature to 400 °C and the temperature-dependent effective thermal conductivity of $Ge_2Sb_2Te_5$ (GST) (including a similar capping layer) from ref 23 (solid circles). The measurement laser spot size is ∼10 μm, and the SL measurements are averaged from three locations on the same sample. (d) Measured total thermal resistance of 4/1 nm/nm superlattice with increasing number of periods, from 2 to 17 at room temperature (2 periods = 4 internal interfaces, including the bottom Sb_2Te_3 seed layer = 14 nm thick, etc.). The inverse of the slope of the linear fit estimates the intrinsic thermal conductivity of the SL, and the y intercept yields the sum of thermal boundary resistance between SL/TiN at the top and SL/Si at the bottom.

their temperature- and period-dependent cross-plane thermal conductivity. These measurements uncover a minimum thermal conductivity and a transition from coherent, wave-like phonon transport to quasi-ballistic phonon transport around the 3/1 nm/nm period. Thickness-dependent measurements also reveal the thermal boundary resistance between SL-PCM and TiN, a typical PCM electrode material. Finally, we report electrical resistivity measurements of 4/1 nm/nm Sb_2Te_3/GeTe SLs, revealing a strong and nearly 2000-fold anisotropy between the cross-plane and in-plane directions.

The cross-plane thermal measurements are carried out using time-domain thermoreflectance (TDTR),[17] which is shown with the prototypical SL stack in Figure 1a. TDTR uses a pump laser that repeatedly heats the top metal surface (here Pt) and a probe laser that measures its temperature. Modulating the pump laser beam from 1 to 10 MHz allows changing its penetration depth into the SL stack and the Si substrate. The measured thermal decay trace is fit to the exact solution of the radial-symmetric heat diffusion equation of the system, enabling the extraction of thermal conductivity and interface thermal resistances within the SL, as well as the thermal boundary resistance of the SL interface with TiN. (Additional details are in the Supporting Information Section 1 and in Figure S1.) In addition, we equip our TDTR system with a high vacuum heating stage to enable temperature-dependent measurements.

The Sb_2Te_3/GeTe SLs used in this work are carefully prepared using radio frequency (RF) magnetron sputtering, followed by transmission electron microscopy (TEM), as

shown in Figure 1b. As a pretreatment for the (poly)crystalline Sb_2Te_3/GeTe deposition, a 10 min Ar plasma cleaning process is performed on a silicon wafer with high resistivity, followed by 4 nm Sb_2Te_3 seed layer deposition at room temperature (RT). This *in situ* cleaning process is used to remove carbon residues and any native oxide on the substrate surface and is also essential for depositing PCM films on the bottom electrode of PCM devices to produce better interfaces.[12] The temperature in the chamber is then elevated to 180 °C without breaking vacuum, and the alternating multilayers of GeTe and Sb_2Te_3 are deposited at a pressure of 4 mTorr.

Cross-sectional high-angle annular dark field (HAADF) scanning transmission electron microscope (STEM) images of the resulting SL (Figure 1b) reveal sharp interfaces with clear van der Waals-like (vdW-like) gaps. Although alternating thin layers of Sb_2Te_3 and GeTe were deposited, the STEM images show a reconfiguration of the superlattice into 5-atom layers of Sb_2Te_3 and odd-numbered (7-, 9-, or 11-atom) layers of $Ge_xSb_yTe_z$ during the sputter deposition at elevated temperature.[18−20] However, a nearly perfect alignment of all vdW-like gaps parallel to the substrate is maintained, as evident from the STEM. We also note the presence of (some) stacking faults and other interfacial defects.[21] These unique structural attributes are expected to play a role in cross-plane electrical and thermal transport, as described below. We cap the SL stacks *in situ* with 10 nm of TiN, the same material used for PCM electrodes, followed by a layer of 70 nm Pt as a reflective transducer to enable TDTR measurements.[22]
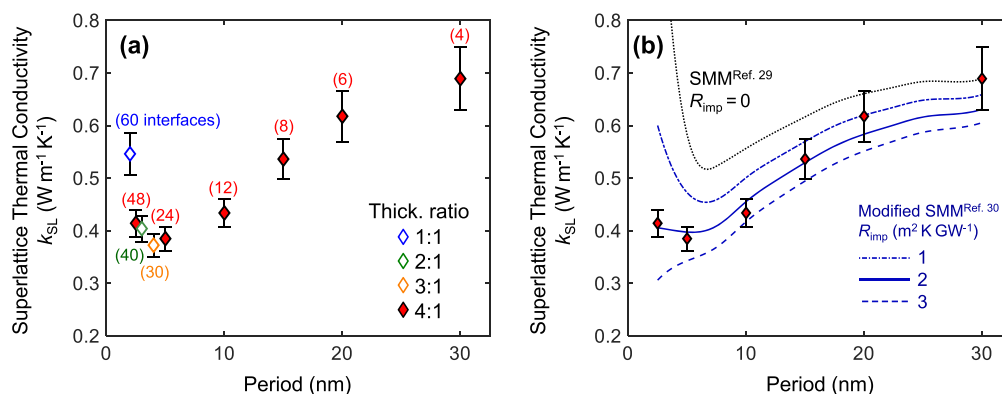
Figure 2. (a) Measured cross-plane thermal conductivity of 60 nm thick Sb_2Te_3/GeTe superlattice (SL) films as a function of the period size ranging from 1/1 to 24/6 nm/nm and of varying thickness ratios at room temperature. Red solid diamonds represent samples with a 4:1 thickness ratio (i.e., Sb_2Te_3/GeTe 4/1, 8/2 nm/nm, etc.). Open blue, green, and orange diamonds correspond to 1/1, 2/1, and 3/1 nm/nm periods, respectively. The numbers in parentheses indicate the total number of internal interfaces in the respective SL-PCM stacks. (b) Data for the measured cross-plane thermal conductivity of the SL-PCM with a 4:1 thickness ratio of Sb_2Te_3/GeTe (red diamonds) and fits using the Simkin–Mahan model (SMM)[29] (dotted black line) and modified SMM[30] (dotted blue lines). The fits are obtained using a fixed phonon mean free path of ~9.4 nm while the contribution of imperfections to thermal boundary resistance per interface, R_{imp}, is varied from 0 to 3 m^2 K GW^{-1}. The best-fit curve to the experimental data corresponds to $R_{imp} = 2$ m^2 K GW^{-1} with a bulk mean free path of 9.4 nm. The error bars of the k_{SL} data are calculated using a previously described approach.[22]

Figure 1c displays our measured effective cross-plane thermal conductivity of a ~60 nm SL with 12 deposited periods of 4 nm Sb_2Te_3 and 1 nm GeTe, with a 10 nm TiN capping layer, from RT to 400 °C. This effective thermal conductivity includes the contribution from the thermal resistances of the SL layers as well as the thermal boundary resistance at the SL/TiN and SL/Si interfaces. The SL is polycrystalline as-deposited at 180 °C, and the overall SL stack has a larger effective thermal conductivity (at RT) (0.29 ± 0.02 W m^{-1} K^{-1}) than that of as-deposited amorphous GST (~0.17 $Wm^{-1}K^{-1}$ for 60-nm a-GST with a similar capping layer).[24] However, the thermal conductivity of GST sharply increases at ~150 °C during the transition to its face-centered cubic (fcc) phase and continues to increase up to ~1.05 W m^{-1} K^{-1} at the onset of the transition to its hexagonal polycrystalline phase at 200 °C.[23] The thermal conductivity of hexagonal-GST then slightly increases up to ~1.24 W m^{-1} K^{-1} at 350 °C.

In contrast, the cross-plane thermal conductivity of our as-deposited polycrystalline SL film increases only slightly with temperature, from 0.29 W m^{-1} K^{-1} at RT to a maximum of 0.47 ± 0.05 W m^{-1} K^{-1} at ~400 °C. This is attributed to a slightly increasing contribution of phonon transport and electron-phonon coupling across the SL interfaces with rising temperature.[24,25] The effective cross-plane thermal conductivity of the SL stack is up to four times lower than that of the polycrystalline GST phases annealed at high temperature, which is primarily attributed to the strong role of the interfaces and vdW-like gaps within the SL. In addition, the as-deposited polycrystalline SL films may have a smaller grain size than the annealed GST (as-deposited amorphous), which could also partially contribute to the measured thermal conductivity difference previously described.

Next, we wish to quantify the thermal conductivity of the Sb_2Te_3/GeTe SL itself and the thermal boundary resistance (TBR) between the SL and the TiN electrode, $R_{SL/TiN}$. These thermal resistances can have a large impact on the temperature increase within SL-PCMs and may shed light on the underlying switching mechanism in these memory devices. For this purpose, we designed a set of ~14, 29, 59, and 89 nm thick samples composed of repeating 1/4 nm/nm GeTe/

Sb_2Te_3 layers on top of the 4 nm Sb_2Te_3 seed layer. The top TiN/Pt capping and bottom 4 nm Sb_2Te_3 seed layers on the silicon wafer are identical for all samples. The total thermal resistances of these SL films, R_{tot}, are measured using TDTR at RT and plotted versus the film thickness in Figure 1d. The slope of the linear regression for R_{tot} can be used to estimate the intrinsic cross-plane thermal conductivity of the SL, $k_{SL} \approx 0.41 \pm 0.04$ W m^{-1} K^{-1}, at RT.

The vertical intercept as the number of film interfaces approaches zero yields the TBR between the TiN capping layer and the SL-PCM film, including a smaller contribution from the SL/Si interface, $R_{SL/TiN+SL/Si} \approx 52.4$ m^2 K GW^{-1}, because the TDTR signal is more sensitive to the top interface with TiN than to the bottom interface with the Si substrate. To confirm this, we conducted an exact fitting process to separately estimate $R_{SL/TiN} = 41.7 \pm 10.8$ m^2 K GW^{-1}. (See the Supporting Information Section 2, Figure S2, and Table S1). This result is ~47% larger than what has been reported between TiN and fcc-GST, $R_{GST/TiN} \approx 28$ m^2 K GW^{-1}.[25] More detailed interface characterization would be needed to explain this difference, but this could be partially attributed to the different deposition temperatures of our SL-PCM films (~180 °C), whereas the fcc-crystalline interface could form a rougher interface compared with an amorphous $Ge_2Sb_2Te_5$ film. In Supporting Information Section 3, we have also detailed a theoretical analysis that indicates that the acoustic velocity of the SL film could be suppressed by ~10% due to the creation of minibands and a flattened phonon dispersion spectrum in SLs.[26] This alone could account for ~27% larger thermal resistance between the SL film and TiN compared with GST and TiN.

To better understand the switching mechanisms and energy transport at the interfaces of SL-PCM, we have conducted systematic thermal characterization of ~60 nm thick films with different size periods and thickness ratios (t.r.) of Sb_2Te_3/GeTe (Figure 2). All films were capped *in situ* with 10 nm thick TiN layers. The SL-PCM period sizes of Sb_2Te_3/GeTe are 24/6, 16/4, 12/3, 8/2, 4/1, and 2/0.5 nm/nm (all with t.r. of 4:1), 3/1 nm/nm (t.r. 3:1), 2/1 nm/nm (t.r. 2:1), and 1/1 nm/nm (t.r. 1:1). As shown in Figure 2a, the cross-plane
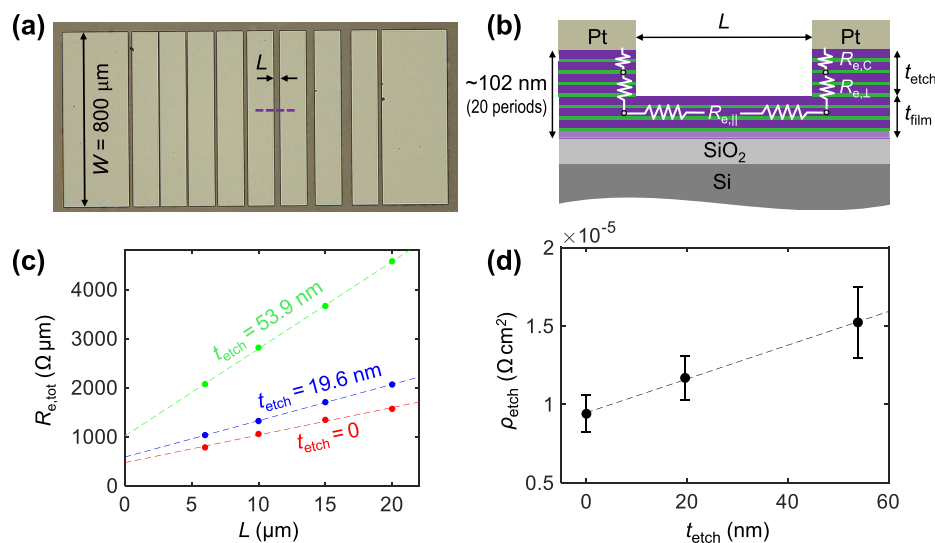
Figure 3. Electrical characterization of Sb_2Te_3/GeTe superlattices with a 4/1 nm/nm period. (a) Top-view optical image of the transfer length method (TLM) structure, where L is the distance between the Pt contact pads and W is the width of each contact pad. (b) Schematic cross-section of the modified TLM (M-TLM) along the dashed line in panel (a), with ~82 nm thick Pt contact pads and a ~100 nm thick Sb_2Te_3/GeTe film with a 4/1 nm/nm period on thermally grown SiO_2 (~110 nm). (c) Measured electrical resistance, $R_{e,tot} = 2R_{e,C} + 2R_{e,\perp} + R_{e,\parallel}$, versus distance, L, between neighboring contact pads for varying SL film etched depths at room temperature. (d) Calculated total area-specific resistance (including the Pt/SL contact resistance), ρ_{etch}, as a function of the etched depth, t_{etch}. Each data point is averaged from the contact resistivities of five M-TLM devices with the same etch depth. The errors due to the fabrication uncertainties are calculated using a Monte Carlo method.[34]

thermal conductivity of SL-PCM films decreases from 0.69 ± 0.06 W m^{-1} K^{-1} for a 24/6 nm/nm period (four internal interfaces) to 0.37 ± 0.03 W m^{-1} K^{-1} for a 3/1 nm/nm period (30 internal interfaces). We note that the thermal conductivity of the SLs shown in Figure 2a excludes the contribution of the TiN capping layer and Si substrate (see Supporting Information Section 2) and thus exclusively represents the thermal transport in SL-PCM films. It is notable that the theoretical minimum lattice thermal conductivity for these materials,[27] $k_{min} \approx 0.31$ W m^{-1} K^{-1} (see Supporting Information Section 4), is only ~18% smaller than the minimum thermal conductivity of the 3/1 nm/nm period (30 interfaces) SL film. Interestingly, the measured thermal conductivity of our SLs increases again for shorter periods of 3/1, 2/1, and 1/1 nm/nm, corresponding to 40, 48, and 60 interfaces, respectively. This counterintuitive trend suggests a transition of phonon transport behavior from the quasi-ballistic regime (>4 nm periods) to a wave-like, quasi-coherent regime (2, 2.5, and 3 nm periods), a phenomenon typically observed in high-quality SL films.[28]

To model this observed thermal conductivity behavior of our Sb_2Te_3/GeTe SLs, we use the Simkin–Mahan model (SMM)[29] with a correction for imperfections at the interfaces,[30] detailed as follows. (Also see Supporting Information Section 5.) The main input parameters to the SMM are the mass ratio of lattice units, the number of lattices consisting of one period of Sb_2Te_3/GeTe, and the bulk phonon mean free path scaled by the lattice constant. We first estimate the bulk phonon mean free path λ in the SL from conventional kinetic theory, $\lambda \approx 3k/(C_v v)$, where k is the phonon thermal conductivity obtained by averaging the bulk thermal conductivity of Sb_2Te_3 and GeTe (with a 4:1 thickness ratio) in the cross-plane direction, C_v is the volumetric specific heat, and v is the average sound velocity (see Supporting Information Section 3 for detailed calculation), yielding $\lambda \approx 1$ nm. However, this mean free path is shorter than our SL

periods, and thus this kinetic theory estimate cannot be applied to understand the observed wave-like phonon behavior shown in Figure 2a.

For additional insight, we recall that layered materials are strongly anisotropic, which could lead to a significant underestimation of the phonon mean free path by kinetic theory[15,31] due to the change in the phonon density of states in the different directions of the lattice. In addition, time-resolved measurements have suggested that phonons could have relatively longer lifetimes in Sb_2Te_3/GeTe SL films.[32] Therefore, to model the experimentally observed thermal conductivity trend (Figure 2a), we use the "modified" SMM[30] (M-SMM) in Figure 2b by employing two free parameters, the bulk phonon mean free path of the SL and the TBR originating from imperfections at SL interfaces. Using the M-SMM, we first determine the best fit (blue solid line) to our experimental data (red solid diamonds representing 24/6, 16/4, 12/3, 8/2, 4/1, and 2/0.5 nm/nm; t.r. 4:1 for Sb_2Te_3/GeTe) with $\lambda = 9.4$ nm and the thermal boundary resistance per interface due to the inelastic scattering caused by imperfections alone, $R_{imp.} = 2$ m^2 K GW^{-1}. Thus the M-SMM with a longer mean free path than kinetic theory better predicts the behavior of the thermal conductivity of our SL-PCM films. This suggests that the mean free path along the cross-plane (c axis) is larger than the one obtained from the simple kinetic theory, which has also been previously observed in similar layered materials such as MoS_2 and graphite.[15,31]

Next, we model the thermal conductivities with a fixed $\lambda = 9.4$ nm while varying R_{imp} from 0 to 3 m^2 K GW^{-1}. We note that for the fits in Figure 2b, we only use the SLs with t.r. 4:1 of Sb_2Te_3/GeTe, where the data for the SL with the largest size period 24/6 nm/nm is available; this is to minimize the impact of the TBR between SL interfaces. It is interesting to note that the fit for R_{imp}= 0 (using the SMM) in Figure 2b represents perfect internal interfaces of Sb_2Te_3/GeTe and captures the trend in the experimental thermal conductivity data of SLs in

Figure 2a; however, this fit clearly overestimates the thermal conductivity for smaller SL periods. By setting R_{imp} = 1 to 2 m^2 K GW^{-1}, our M-SMM closely captures the experimental thermal conductivity data. Such low R_{imp} values indicate the overall high-quality interfaces of our SLs (further detailed in Supporting Information Section 5 and in Figure S3), with any contributions most likely arising from stacking faults[18,33] that are apparent in Figure 1b. We further note that the fitted R_{imp} values agree well with the molecular dynamics simulation results for the TBR per interface (1 to 2 m^2 K GW^{-1}) due to imperfections at the different atomic layers of Bi$_2$Te$_3$.[34]

We now turn to the electrical resistivity characterization of our SL films, which may also impact their programming in SL-PCM data storage devices. For the in-plane electrical resistivity measurements of thin films, the standard transfer length method (TLM) is usually employed,[35] as shown in Figure 3a. This measurement is sensitive to the in-plane electrical resistivity, $\rho_{\parallel}$, and the electrical contact resistivity with the metal pads, ρ_C. For cross-plane electrical resistivity measurements, we utilize a modified TLM (M-TLM), which uses mesa structures to simultaneously determine the cross-plane electrical resistivity.[36] To fabricate the M-TLM structure, we etch into the SL film between the two metal contacts (here Pt), as shown in Figure 3b. (Also see Supporting Information Section 6.) This will increase the contribution of the cross-plane electrical resistance, $R_{e\perp}$, that is proportional to the etched depth, t_{etch}.

The contact and cross-plane resistivities of the SL film can be estimated from simultaneously fitting the measured electrical resistance as a function of the contact spacing and etch depth in the modified TLM devices. Figure 3c shows the fitting line of the electrical resistance in each M-TLM device with an SL formed by 4 nm Sb$_2$Te$_3$ and 1 nm GeTe deposition, and Figure 3d shows the total area-specific resistance, ρ_{etch} (including the SL/metal contact resistance), corresponding to the amount of the etched depth. The slope in Figure 3d represents the cross-plane electrical resistivity of these SLs, $\rho_{\perp}$ ≈ 1.1 ± 0.35 Ω cm at RT. The in-plane electrical resistivity is estimated as $\rho_{\parallel}$ ≈ 5.8 ± 0.3 × 10^{-4} Ω cm from the lateral TLM. The error bars of $\rho_{\parallel}$ and $\rho_{\perp}$ are calculated using a Monte Carlo approach,[37] propagated from the uncertainties in the metal contact width and spacing (±0.5 μm) as well as the etch depth (±2 nm). We note that the measured electrical resistances for different etched depths of SL films show linearity (Figure 3c) across large distances of neighboring contact spacing (up to 20 μm), indicating the good uniformity of our sputtered SLs over a large area.

Our measured in-plane electrical resistivity is similar to that previously reported in-plane for such SLs[38] and to that of crystalline GeTe,[39] but is smaller than that of crystalline Sb$_2$Te$_3$,[40] and nearly 2000 times smaller than the SL cross-plane resistivity. This strong anisotropy in the electrical transport is in close agreement with previously reported data[41] for such SL films. The large anisotropy is not surprising in these layered SL materials (see Supplementary Table S2), with covalent bonds in-plane and numerous weak vdW-like bonds and some stacking disorder in the cross-plane direction.[41−43] Some charge accumulation or depletion in adjacent SL layers (with smaller and larger band gaps, respectively)[44] could also contribute to the anisotropy of electrical resistivity in these films and could be the subject of future exploration.

We also note how these SL resistivity values compare to those in a-GST (>10^2 Ω cm), fcc-GST (∼0.1 Ω cm), and hexagonal-GST (∼10^{-3} Ω cm) near RT.[45] In other words, the cross-plane resistivity of the SL is larger than that of the crystalline phases of GST, whereas the in-plane resistivity of the SL is slightly smaller than that of the hexagonal-GST. The in-plane SL resistivity can also be used to estimate the *electronic* contribution to the in-plane thermal conductivity with the Wiedemann−Franz law, $k_{e,\parallel}$ ≈ 1.24 W m^{-1} K^{-1}, which represents a lower bound. The total in-plane thermal conductivity of the SL could be up to ∼5 W m^{-1} K^{-1} at RT, including the phonon component, based on the in-plane thermal conductivity of both crystalline GeTe[39] and Sb$_2$Te$_3$[40] (but it is likely to be somewhat smaller for the SL due to finite size effects in our ultrathin films). This means that our SLs with 4/1 nm/nm periods have greater than four-fold (and possibly up to 16-fold) thermal anisotropy between the in-plane and cross-plane directions.

In summary, we reported the electrical and thermal transport characterization of SL-PCMs with Sb$_2$Te$_3$/GeTe alternating layers. The measured in-plane and cross-plane electrical resistivities of the SLs indicate a very anisotropic structure, which can largely impact the electric field and the resulting heat generation in SL-based PCM devices. We also observe up to approximately four times lower effective cross-plane thermal conductivity of (poly)crystalline Sb$_2$Te$_3$/GeTe SLs compared with crystalline GST due to the presence of SL interfaces. These could play a strong role in the reduction of the SL-PCM programing current compared with conventional PCM based on GST. We also observed a transition from quasi-coherent to quasi-ballistic phonon transport as we varied the period of Sb$_2$Te$_3$/GeTe films (from 1/1 to 24/6 nm/nm), with a minimum thermal conductivity observed around the 3/1 nm/nm period. Future work could provide additional in-plane and cross-plane thermal and electrical measurements of SLs at cryogenic and high temperatures to further our understanding of transport physics in such materials.

■ ASSOCIATED CONTENT

Ⓢ Supporting Information

The Supporting Information is available free of charge at https://pubs.acs.org/doi/10.1021/acs.nanolett.1c00947.

Additional details of the time domain thermoreflectance measurement method, sensitivity analysis, theoretical calculation of thermal boundary resistance, theoretical estimation of minimum thermal conductivity, additional details of the thermal modeling, and additional details and benchmarking of the electrical resistivity measurement (PDF)

■ AUTHOR INFORMATION

Corresponding Author

Kenneth E. Goodson − Department of Mechanical Engineering and Department of Materials Science & Engineering, Stanford University, Stanford, California 94305, United States; Email: goodson@stanford.edu

Authors

Heungdong Kwon − Department of Mechanical Engineering, Stanford University, Stanford, California 94305, United States; ● orcid.org/0000-0002-2548-3120

Asir Intisar Khan − *Department of Electrical Engineering, Stanford University, Stanford, California 94305, United States;* ⓘ orcid.org/0000-0003-4635-4667

Christopher Perez − *Department of Mechanical Engineering, Stanford University, Stanford, California 94305, United States;* ⓘ orcid.org/0000-0002-9628-2027

Mehdi Asheghi − *Department of Mechanical Engineering, Stanford University, Stanford, California 94305, United States*

Eric Pop − *Department of Electrical Engineering and Department of Materials Science & Engineering, Stanford University, Stanford, California 94305, United States;* ⓘ orcid.org/0000-0003-0436-8534

Complete contact information is available at:
https://pubs.acs.org/10.1021/acs.nanolett.1c00947

Author Contributions

H.K. and A.I.K. conducted the thermal and electrical measurements. A.I.K. and H.K. performed the film depositions. All authors contributed to the discussion of the experimental results and the writing of the manuscript.

Notes

The authors declare no competing financial interest.

■ REFERENCES

(1) Raoux, S.; Xiong, F.; Wuttig, M.; Pop, E. Phase Change Materials and Phase Change Memory. *MRS Bull.* **2014**, *39* (8), 703−710.

(2) Sebastian, A.; Le Gallo, M.; Burr, G. W.; Kim, S.; BrightSky, M.; Eleftheriou, E. Tutorial: Brain-Inspired Computing Using Phase-Change Memory Devices. *J. Appl. Phys.* **2018**, *124* (11), 111101.

(3) Wong, H.-S. P.; Raoux, S.; Kim, S.; Liang, J.; Reifenberg, J. P.; Rajendran, B.; Asheghi, M.; Goodson, K. E. Phase Change Memory. *Proc. IEEE* **2010**, *98* (12), 2201−2227.

(4) Egami, T.; Johguchi, K.; Yamazaki, S.; Takeuchi, K. Investigation of Multi-Level-Cell and SET Operations on Super-Lattice Phase Change Memories. *Jpn. J. Appl. Phys.* **2014**, *53* (4S), 04ED02.

(5) Tominaga, J.; Fons, P.; Kolobov, A.; Shima, T.; Chong, T. C.; Zhao, R.; Lee, H. K.; Shi, L. Role of Ge Switch in Phase Transition: Approach Using Atomically Controlled Sb$_2$Te$_3$/GeTe Superlattice. *Jpn. J. Appl. Phys.* **2008**, *47* (7), 5763−5766.

(6) Simpson, R. E.; Fons, P.; Kolobov, A. V.; Fukaya, T.; Krbal, M.; Yagi, T.; Tominaga, J. Interfacial Phase-Change Memory. *Nat. Nanotechnol.* **2011**, *6* (8), 501−505.

(7) Kim, W.; BrightSky, M.; Masuda, T.; Sosa, N.; Kim, S.; Bruce, R.; Carta, F.; Fraczak, G.; Cheng, H. Y.; Ray, A.; Zhu, Y.; Lung, H. L.; Suu, K.; Lam, C. ALD-Based Confined PCM with a Metallic Liner toward Unlimited Endurance. *2016 IEEE International Electron Devices Meeting (IEDM)* **2016**, 4.2.1−4.2.4.

(8) Fong, S. W.; Sood, A.; Chen, L.; Kumari, N.; Asheghi, M.; Goodson, K. E.; Gibson, G. A.; Wong, H.-S. P. Thermal Conductivity Measurement of Amorphous Dielectric Multilayers for Phase-Change Memory Power Reduction. *J. Appl. Phys.* **2016**, *120* (1), 015103.

(9) Fong, S. W.; Neumann, C. M.; Yalon, E.; Rojo, M. M.; Pop, E.; Wong, H.-S. P. Dual-Layer Dielectric Stack for Thermally Isolated Low-Energy Phase-Change Memory. *IEEE Trans. Electron Devices* **2017**, *64* (11), 4496−4502.

(10) Ahn, C.; Fong, S. W.; Kim, Y.; Lee, S.; Sood, A.; Neumann, C. M.; Asheghi, M.; Goodson, K. E.; Pop, E.; Wong, H.-S. P. Energy-Efficient Phase-Change Memory with Graphene as a Thermal Barrier. *Nano Lett.* **2015**, *15* (10), 6809−6814.

(11) Neumann, C. M.; Okabe, K. L.; Yalon, E.; Grady, R. W.; Wong, H.-S. P.; Pop, E. Engineering Thermal and Electrical Interface Properties of Phase Change Memory with Monolayer MoS$_2$. *Appl. Phys. Lett.* **2019**, *114* (8), 082103.

(12) Khan, A. I.; Kwon, H.; Islam, R.; Perez, C.; Chen, M. E.; Asheghi, M.; Goodson, K. E.; Wong, H.-S. P.; Pop, E. Two-Fold Reduction of Switching Current Density in Phase Change Memory Using Bi$_2$Te$_3$ Thermoelectric Interfacial Layer. *IEEE Electron Device Lett.* **2020**, *41* (11), 1657−1660.

(13) Ren, K.; Cheng, Y.; Chen, X.; Ding, K.; Lv, S.; Yin, W.; Guo, X.; Ji, Z.; Song, Z. Carbon Layer Application in Phase Change Memory to Reduce Power Consumption and Atomic Migration. *Mater. Lett.* **2017**, *206*, 52−55.

(14) Aryana, K.; Gaskins, J. T.; Nag, J.; Stewart, D. A.; Bai, Z.; Mukhopadhyay, S.; Read, J. C.; Olson, D. H.; Hoglund, E. R.; Howe, J. M.; Giri, A.; Grobis, M. K.; Hopkins, P. E. Interface Controlled Thermal Resistances of Ultra-Thin Chalcogenide-Based Phase Change Memory Devices. *Nat. Commun.* **2021**, *12* (1), 774.

(15) Sood, A.; Xiong, F.; Chen, S.; Cheaito, R.; Lian, F.; Asheghi, M.; Cui, Y.; Donadio, D.; Goodson, K. E.; Pop, E. Quasi-Ballistic Thermal Transport Across MoS$_2$ Thin Films. *Nano Lett.* **2019**, *19* (4), 2434−2442.

(16) Boniardi, M.; Boschker, J. E.; Momand, J.; Kooi, B. J.; Redaelli, A.; Calarco, R. Evidence for Thermal-Based Transition in Super-Lattice Phase Change Memory. *Phys. Status Solidi RRL* **2019**, *13* (4), 1800634.

(17) Jiang, P.; Qian, X.; Yang, R. Tutorial: Time-Domain Thermoreflectance (TDTR) for Thermal Property Characterization of Bulk and Thin Film Materials. *J. Appl. Phys.* **2018**, *124* (16), 161103.

(18) Momand, J.; Wang, R.; Boschker, J. E.; Verheijen, M. A.; Calarco, R.; Kooi, B. J. Dynamic Reconfiguration of van Der Waals Gaps within GeTe-Sb$_2$Te$_3$ Based Superlattices. *Nanoscale* **2017**, *9* (25), 8774−8780.

(19) Lotnyk, A.; Hilmi, I.; Ross, U.; Rauschenbach, B. Van Der Waals Interfacial Bonding and Intermixing in GeTe-Sb$_2$Te$_3$-Based Superlattices. *Nano Res.* **2018**, *11* (3), 1676−1686.

(20) Kowalczyk, P.; Hippert, F.; Bernier, N.; Mocuta, C.; Sabbione, C.; Batista-Pessoa, W.; Noé, P. Impact of Stoichiometry on the Structure of van Der Waals Layered GeTe/Sb$_2$Te$_3$ Superlattices Used in Interfacial Phase-Change Memory (IPCM) Devices. *Small* **2018**, *14* (24), 1704514.

(21) Wang, R.; Bragaglia, V.; Boschker, J. E.; Calarco, R. Intermixing during Epitaxial Growth of van Der Waals Bonded Nominal GeTe/Sb$_2$Te$_3$ Superlattices. *Cryst. Growth Des.* **2016**, *16* (7), 3596−3601.

(22) Kwon, H.; Perez, C.; Kim, H. K.; Asheghi, M.; Park, W.; Goodson, K. E. Thermal Interface Enhancement via Inclusion of an Adhesive Layer Using Plasma-Enhanced Atomic Layer Deposition. *ACS Appl. Mater. Interfaces* **2021**, *13*, 21905.

(23) Reifenberg, J. P.; Panzer, M. A.; Kim, S.; Gibby, A. M.; Zhang, Y.; Wong, S.; Wong, H. S. P.; Pop, E.; Goodson, K. E. Thickness and Stoichiometry Dependence of the Thermal Conductivity of GeSbTe Films. *Appl. Phys. Lett.* **2007**, *91* (11), 111904.

(24) Yang, Y.; Hamann, H. F.; Asheghi, M. Thermal Conductivity Measurements and Modeling of Phase-Change Ge$_2$Sb$_2$Te$_5$ Materials. *Nanoscale Microscale Thermophys. Eng.* **2009**, *13* (2), 88−98.

(25) Lee, J.; Bozorg-Grayeli, E.; Kim, S.; Asheghi, M.; Philip Wong, H. S.; Goodson, K. E. Phonon and Electron Transport through

Ge$_2$Sb$_2$Te$_5$ Films and Interfaces Bounded by Metals. *Appl. Phys. Lett.* **2013**, *102* (19), 191911.

(26) Tamura, S.-i.; Tanaka, Y.; Maris, H. J. Phonon Group Velocity and Thermal Conduction in Superlattices. *Phys. Rev. B: Condens. Matter Mater. Phys.* **1999**, *60* (4), 2627−2630.

(27) Cahill, D. G.; Watson, S. K.; Pohl, R. O. Lower Limit to the Thermal Conductivity of Disordered Crystals. *Phys. Rev. B: Condens. Matter Mater. Phys.* **1992**, *46* (10), 6131−6140.

(28) Ravichandran, J.; Yadav, A. K.; Cheaito, R.; Rossen, P. B.; Soukiassian, A.; Suresha, S. J.; Duda, J. C.; Foley, B. M.; Lee, C. H.; Zhu, Y.; Lichtenberger, A. W.; Moore, J. E.; Muller, D. A.; Schlom, D. G.; Hopkins, P. E.; Majumdar, A.; Ramesh, R.; Zurbuchen, M. A. Crossover from Incoherent to Coherent Phonon Scattering in Epitaxial Oxide Superlattices. *Nat. Mater.* **2014**, *13* (2), 168−172.

(29) Simkin, M. V.; Mahan, G. D. Minimum Thermal Conductivity of Superlattices. *Phys. Rev. Lett.* **2000**, *84* (5), 927−930.

(30) Yang, B.; Chen, G. Partially Coherent Phonon Heat Conduction in Superlattices. *Phys. Rev. B: Condens. Matter Mater. Phys.* **2003**, *67* (19), 195311.

(31) Zhang, H.; Chen, X.; Jho, Y. D.; Minnich, A. J. Temperature-Dependent Mean Free Path Spectra of Thermal Phonons Along the c-Axis of Graphite. *Nano Lett.* **2016**, *16* (3), 1643−1649.

(32) Makino, K.; Saito, Y.; Fons, P.; Kolobov, A. V.; Nakano, T.; Tominaga, J.; Hase, M. Coherent Phonon Study of (GeTe)$_l$(Sb$_2$Te$_3$)$_m$ Interfacial Phase Change Memory Materials. *Appl. Phys. Lett.* **2014**, *105* (15), 151902.

(33) Hopkins, P. E. Thermal Transport across Solid Interfaces with Nanoscale Imperfections: Effects of Roughness, Disorder, Dislocations, and Bonding on Thermal Boundary Conductance. *ISRN Mech. Eng.* **2013**, *2013*, 1−19.

(34) Hsieh, I. T.; Huang, M. J. An Investigation into the Thermal Boundary Resistance Associated with the Twin Boundary in Bismuth Telluride. *Nanoscale Microscale Thermophys. Eng.* **2019**, *23* (1), 36−47.

(35) Berger, H. H. Contact Resistance and Contact Resistivity. *J. Electrochem. Soc.* **1972**, *119* (4), 507.

(36) Yang, B.; Liu, W. L.; Liu, J. L.; Wang, K. L.; Chen, G. Measurements of Anisotropic Thermoelectric Properties in Superlattices. *Appl. Phys. Lett.* **2002**, *81* (19), 3588−3590.

(37) Cox, M.; Harris, P.; Siebert, B. R. L. Evaluation of Measurement Uncertainty Based on the Propagation of Distributions Using Monte Carlo Simulation. *Meas. Tech.* **2003**, *46* (9), 824−833.

(38) Cecchi, S.; Zallo, E.; Momand, J.; Wang, R.; Kooi, B. J.; Verheijen, M. A.; Calarco, R. Improved Structural and Electrical Properties in Native Sb$_2$Te$_3$/Ge$_x$Sb$_2$Te$_{3+x}$ van Der Waals Superlattices Due to Intermixing Mitigation. *APL Mater.* **2017**, *5* (2), 026107.

(39) Nath, P.; Chopra, K. L. Thermal Conductivity of Amorphous and Crystalline Ge and GeTe Films. *Phys. Rev. B* **1974**, *10* (8), 3412−3418.

(40) Das, V. D.; Soundararajan, N. Thermoelectric Power and Electrical Resistivity of Crystalline Antimony Telluride (Sb$_2$Te$_3$) Thin Films: Temperature and Size Effects. *J. Appl. Phys.* **1989**, *65* (6), 2332−2341.

(41) Yang, Z.; Xu, M.; Cheng, X.; Tong, H.; Miao, X. Manipulation of Dangling Bonds of Interfacial States Coupled in GeTe-Rich GeTe/Sb$_2$Te$_3$ Superlattices. *Sci. Rep.* **2017**, *7* (1), 17353.

(42) Liu, J.; Okamoto, S.; Van Veenendaal, M.; Kareev, M.; Gray, B.; Ryan, P.; Freeland, J. W.; Chakhalian, J. Quantum Confinement of Mott Electrons in Ultrathin LaNiO$_3$/LaAlO$_3$ Superlattices. *Phys. Rev. B: Condens. Matter Mater. Phys.* **2011**, *83* (17), 161102.

(43) Peng, H.; Xie, C.; Schoen, D. T.; Cui, Y. Large Anisotropy of Electrical Properties in Layer-Structured In$_2$Se$_3$ Nanowires. *Nano Lett.* **2008**, *8* (5), 1511−1516.

(44) Yu, R. H. Tamm states in finite semiconductor superlattices: Influence of accumulation and depletion layers. *Phys. Rev. B: Condens. Matter Mater. Phys.* **1993**, *47* (3), 1379−1382.

(45) Deshmukh, S.; Yalon, E.; Lian, F.; Schauble, K. E.; Xiong, F.; Karpov, I. V.; Pop, E. Temperature-Dependent Contact Resistance to

Nonvolatile Memory Materials. *IEEE Trans. Electron Devices* **2019**, *66* (9), 3816−3821.

Supporting Information

Uncovering Thermal and Electrical Properties of Sb₂Te₃/GeTe Superlattice Films

Heungdong Kwon[1], Asir Intisar Khan[2], Christopher Perez[1], Mehdi Asheghi[1], Eric Pop[2,3], Kenneth E. Goodson[1,3,*]

[1]Dept. of Mechanical Eng., Stanford University, Stanford, CA 94305, U.S.A.

[2]Dept. of Electrical Eng., Stanford University, Stanford, CA 94305, U.S.A.

[3]Dept. of Materials Science & Eng., Stanford University, Stanford, CA 94305, U.S.A.

[*]*E-mail*: goodson@stanford.edu
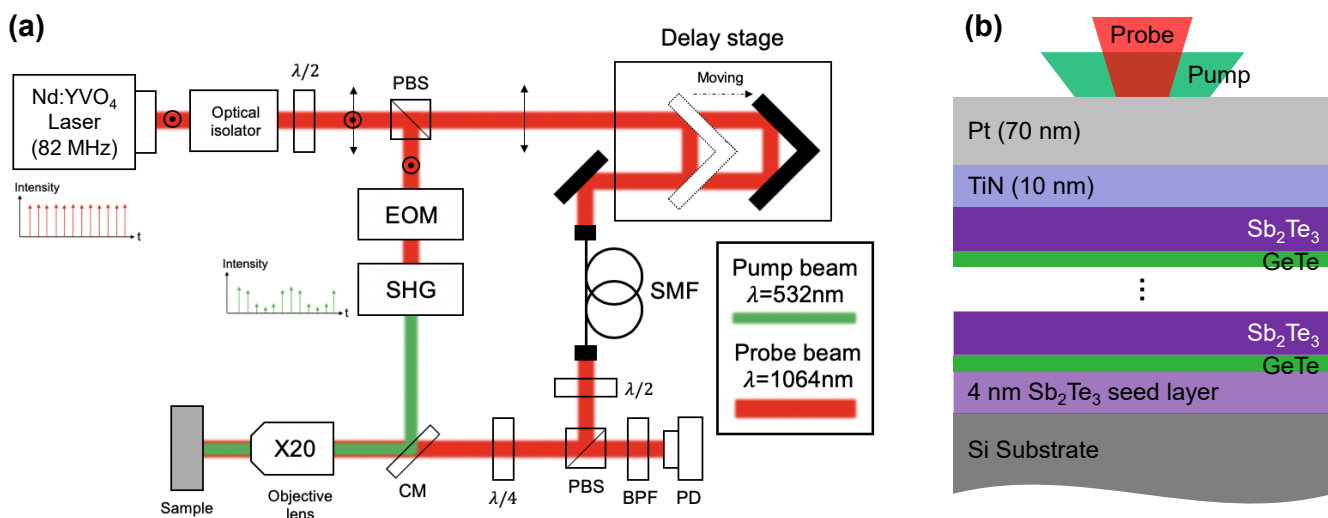
1. Time Domain Thermoreflectance (TDTR)

Figure S1. (a) Schematic of TDTR experiment set-up. (b) Schematic of the film stack used for TDTR measurements of the superlattice type phase change material (SL-PCM). The sample consists of (bottom to top): silicon substrate, 4 nm Sb₂Te₃ seed layer, repeating Sb₂Te₃/GeTe layers, 10 nm TiN capping layer, and 70 nm thick platinum transducer for TDTR measurement.

As depicted in Figure S1, our TDTR set-up use Nd:YVO₄ pulsed laser emitting pulse train with 82 MHz repetition rate. The laser output that passes through an optical isolator is divided into the pump beam and probe beam paths. The pump beam pulse train is modulated with a sinusoidal envelope from 1 MHz to 10 MHz using an electro-optic modulator (EOM) and the 1064 nm wavelength is halved in the second harmonic generator (SHG). The modulated pump laser reflected from the cold mirror (CM) is projected onto the sample to induce modulated surface heating of the platinum transducer layer. The probe beam is time-delayed behind the pump pulse train by using the precise delay stage. The time-delayed probe beam goes through a single mode fiber (SMF) and is reflected on the polarized beam splitter (PBS). The beam is then circularly polarized through the quarter wave plate (λ/4). The reflected probe

laser is detected by a high-speed photodetector (PD). The optical signal is measured by the lock-in amplifier wired to the PD. We monitor the ratio between in- and out-of-phase voltage signals from the lock-in amplifier as a function of the time delay between the pump and probe beams. This ratio signal is fitted with a multilayer heat diffusion model[1] to extract the unknown parameters.
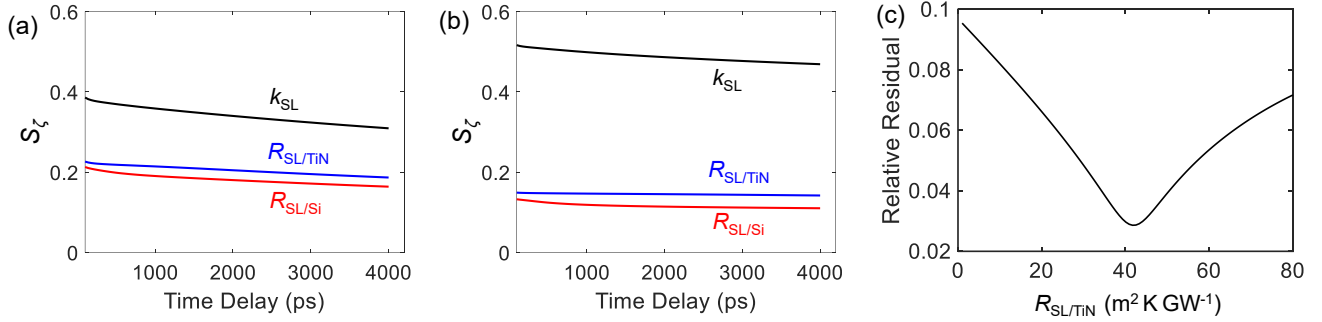
2. Sensitivity Analysis

Figure S2. Measurement sensitivity of the TDTR signal to the thermal conductivity of SL (k_{SL}), to the thermal boundary resistance between TiN capping and SL ($R_{SL/TiN}$), and to the thermal boundary resistance between SL and silicon substrate ($R_{SL/Si}$). The sensitivity analysis is performed on (a) 14 nm and (b) 29 nm thick 4/1 nm/nm Sb$_2$Te$_3$/GeTe SL samples. The 4 MHz heating modulation frequency is used as the frequency in the experiment. (c) For a 29 nm thick sample, the relative residual of the fitting is plotted as a function of the assumed value of $R_{SL/TiN}$.

The sensitivity parameter S_ζ represents the relative change of TDTR output signal (voltage ratio) to the fractional change in a property of interest (ζ). As shown in Figure S2a above, for the thinnest sample (14 nm thick SL), $R_{SL/TiN}$ and $R_{SL/Si}$ have a similar sensitivity coefficient because the heat wave penetrates all the way into the silicon substrate. In other words, they are equally weighted, which means that the thermal conductivity of the SL film bounded by these two interfaces is similarly weighted. Therefore, the TDTR measurement on this sample yields $R_{total}=R_{SL/TiN} + d_{SL}/k_{SL} + R_{SL/Si} \approx 86.1$ m^2 K GW^{-1}, where d_{SL} is the total thickness of the SL. The measured intrinsic thermal conductivity of the SL $k_{SL} \approx 0.41$ W m^{-1} K^{-1} from the slope of the line fitting the total thermal resistances of four samples is used to reduce one unknown parameter in R_{total} (main text Figure 1d). Using the intermediately thick SL (29 nm), of which $R_{SL/TiN}$, k_{SL}, and $R_{SL/Si}$ are sensitive to TDTR signals as seen in Figure S2b, we fit $R_{SL/TiN}$ to minimize the fitting error with the constraint of R_{total} as shown in Figure S2c. The minimum error occurs at $R_{SL/TiN}$ = 41.7 ± 10.8 m^2 K GW^{-1}, confirming $R_{SL/TiN}$ is nearly four times larger than $R_{SL/Si}$, which is ~11.9 m^2 K GW^{-1}.

Properties	Materials			
	TiN	**fcc-Ge$_2$Sb$_2$Te$_5$**	**Sb$_2$Te$_3$**	**GeTe**
ρ [g cm^{-3}]	5.40	6.30	6.51	6.18
C_v [MJ m^{-3} K^{-1}]	3.14 (Ref. 7)	1.34 (Ref. 8)	1.29 (Ref. 9)	1.53 (Ref. 10)
$v_{s,L}$ [m/s]	9638 (Ref. 11)	3190 (Ref. 12)	2757 (c-axis)[Ref. 13]	2670 (c-axis)[Ref. 14]
$k_{bulk,lattice}$ [W m^{-1} K^{-1}]	-	-	0.8 (c-axis)[Ref. 15]	2 (c-axis)[Ref. 15]

Table S1. Summary of the reported values for the density (ρ), volumetric specific heat (C_V), and longitudinal sound velocity ($v_{s,L}$) for TiN, fcc-Ge$_2$Sb$_2$Te$_5$, crystalline Sb$_2$Te$_3$, and crystalline GeTe. For Sb$_2$Te$_3$ and GeTe, the cross-plane (c-axis) longitudinal sound velocity and thermal conductivity data are referred to estimate the phonon mean free path in their superlattices.

3. Theoretical Calculation of Thermal Boundary Resistance (TBR)

The result shows ~47 % larger thermal boundary resistance than the reported data[2] between TiN and fcc-Ge$_2$Sb$_2$Te$_5$ (GST), $R_{GST/TiN} \approx 28$ m^2 K GW^{-1}. Several studies have indicated that the cross-plane acoustic velocity of the SL film could be suppressed significantly due to the creation of minibands and flattened phonon dispersion spectra in SLs.[3,4] To explain the larger $R_{SL/TiN}$ compared to $R_{GST/TiN}$, we calculate the theoretical TBR using the Diffuse Mismatch Model (DMM) with a gray approximation.[5]

$$R = \frac{C_{v,1}}{4\pi} \left(\frac{v_2 C_{v,2}}{v_1 C_{v,1} + v_2 C_{v,2}} \right)^{-1}$$

where C_v is the volumetric specific heat, v is the sound velocity, and the subscripts indicate the material on either side of the interface. The material properties used in the TBR calculation are presented in Table S1. The volumetric specific heat in Table S1 is calculated from the density in the table and the molecular specific heat given by the corresponding references. For the sound velocity in the model, we use the values of longitudinal sound velocity. Although this simplified model cannot predict an accurate TBR compared to the DMM using a full phonon dispersion, the approximation can provide insight into the trend of TBRs. For the cross-plane sound velocity of the SL film, we use the following equation given in Ref 6.

$$v_{SL} = \frac{d}{\sqrt{\dfrac{d_1^2}{v_1^2} + \dfrac{d_2^2}{v_2^2} + \left(\dfrac{Z_1}{Z_2} + \dfrac{Z_1}{Z_2}\right)\dfrac{d_1 d_2}{v_1 v_2}}}$$

where $Z = \rho v$ is the acoustic impedance, d is the period of the SL, and the subscripts indicate the materials on either side of the interface (i.e. Sb$_2$Te$_3$ and GeTe). The estimated effective velocity across the SL is used as the parameter to calculate the thermal boundary resistance between TiN and SL-PCM with the DMM. As expected, the averaged volumetric specific heat (1.32 MJ m^{-3} K^{-1}) and longitudinal acoustic velocity (2739 m/s) of 4/1 nm/nm Sb$_2$Te$_3$/GeTe are not noticeably different from those of fcc-Ge$_2$Sb$_2$Te$_5$ (shown in Table S1), owing to their similar molecular composition. It was observed that the measured longitudinal sound velocity across a Sb$_2$Te$_3$/Bi$_2$Te$_3$ SL is ~10%

reduced from its effective sound velocity.[6] In this study, we use the same scaling factor to estimate the decreased cross-plane longitudinal sound velocity of the 4/1 nm/nm Sb_2Te_3/GeTe film from the effective velocity. The ratio between $R_{SL/TiN}$ and $R_{GST/TiN}$ is then calculated to be ~1.27. Though the ratio of TBRs calculated using the simple DMM model underestimates the experimental values of TBR between SL/TiN relative to the reported data of TBR of fcc-GST/TiN film, we attribute the higher TBR of SL-PCM to the decreased sound velocity in SL film.

4. Minimum Thermal Conductivity

The minimum thermal conductivity model proposed by Cahill *et al*.[16] describes the thermal conductivity of a highly disordered (amorphous) crystal with a random walk motion of vibrational modes, as:

$$k_{min} = \frac{1}{2}\left(\frac{\pi}{6}\right)^{\frac{1}{3}} k_B n_a^{\frac{2}{3}} (v_l + 2v_t)$$

where k_B is the Boltzmann constant, n_a is the atomic number density, v_l is the longitudinal speed of sound, and v_t is the transverse speed of sound. Using this model, the theoretical lower bound of thermal conductivity for superlattices can be estimated.[17] To estimate the minimum thermal conductivity of SL explored in this study, first, we calculate the individual minimum thermal conductivities of Sb_2Te_3 and GeTe respectively, and then the minimum thermal conductivity of SL is estimated with their thickness ratio in the SL period unit. The atomic density is derived using the mass density and molar mass of each material and the sound velocity data of Sb_2Te_3 and GeTe are taken from Ref. 13 and Ref. 14, respectively.

5. Simkin and Mahan model (SMM)

To analyze our experimental data of the cross-plane thermal conductivity of superlattice (SL) films, we employ the Simkin and Mahan model (SMM),[18] which describes thermal transport in the SL films with SL period smaller than the coherence length of phonon. This approach reduces the SL system into a periodic one-dimensional mass-spring chain system where molecular mass of a molecule (e.g. Sb_2Te_3 or GeTe) that comprises the SL is considered. From the calculated band structure determined from the characteristic matrix, we estimate the thermal conductivities of SLs. The input parameters for SMM are the bulk phonon mean free path and the molecular mass ratio between the two materials in the SL. We consider the 4:1 thickness ratio of Sb_2Te_3 and GeTe in one period of SL for our case. However, this model assumes elastic scattering processes at the interface, which cannot account for imperfections or disorder at the interfaces present in our SL films, some of which can be seen in Figure 1b of the main text. Therefore, we modify the SMM as described in Ref. 19 to incorporate the impact of these imperfections. In addition, using the conventional kinetic theory, the estimated phonon mean free path across the SL films is ~1 nm (as explained in the main text), which is shorter than the period of the SL. In this case, SMM cannot predict the experimentally observed thermal conductivity in such SL. Therefore, to obtain a better estimate of phonon mean free path across our SLs, we fit the experimental thermal conductivity data using a modified SMM (M-SMM). The

bulk phonon mean free path across the SL (λ), and the thermal boundary resistances *per interface* due to imperfections acting alone (R_{imp}) are used as the two unknown free parameters, see Figure 2b in the main text.

To obtain further insight, we plot (Figure S3) various thermal resistances of Sb$_2$Te$_3$/GeTe SL films (total thickness 60 nm) with varying period thicknesses for a fixed mean free path of 9.4 nm and four different values of R_{imp} = 0, 1, 2, and 3 m^2 K GW^{-1} (TBR per interface due to imperfections, acting alone). As the TBR due to the imperfection at the interface increases, the total thermal resistance calculated using the modified SMM ($R_{M\text{-}SMM}$) in the SL becomes larger than the thermal resistance estimated by SMM. For R_{imp} ~3 m^2 K GW^{-1} (Figure S3d), a minimum thermal conductivity of SL (a maximum thermal resistance) cannot be observed, because of the dominance of the thermal resistance due to the imperfections in the overall resistance of SL film. This indicates that the phonon coherence phenomena may not be observed in SL films with lower quality interfaces (i.e., higher R_{imp}). At the same time, this further points to the good quality interfaces in our studied SLs.
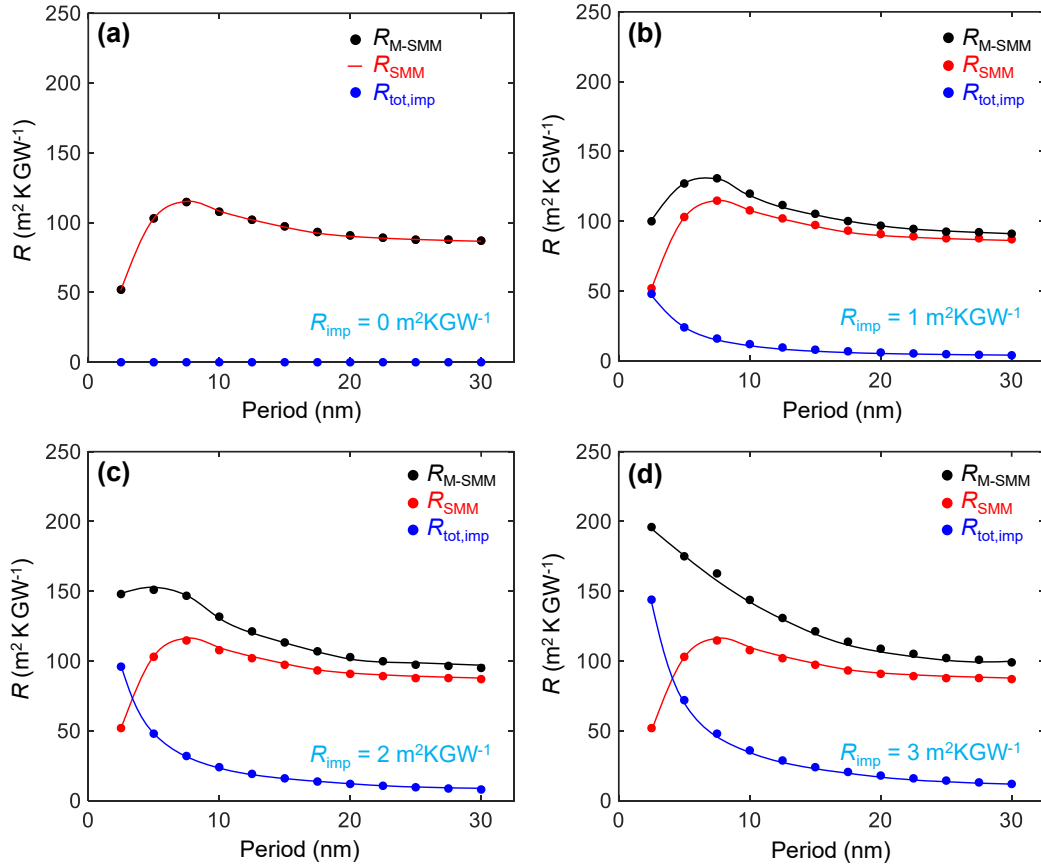

Figure S3. The calculated total thermal resistance of Sb$_2$Te$_3$/GeTe SL using modified SMM $R_{M\text{-}SMM}$ (black), the thermal resistance of SL estimated by SMM R_{SMM} (red), and the total thermal resistance due to imperfections at the interfaces in the SL $R_{tot,imp}$ (blue) as a function of the period thicknesses for varying R_{imp} = (a) 0 m^2 K GW^{-1}, (b) 1 m^2 K GW^{-1}, (c) 2 m^2 K GW^{-1}, and (d) 3 m^2 K GW^{-1}. Here, R_{imp} is the thermal boundary resistance per interface in SL due to imperfections acting alone. $R_{M\text{-}SMM}$ = R_{SMM} + $R_{tot,imp}$ where, $R_{tot,imp}$ = nR_{imp} and n is the total number of internal interfaces within the SL.

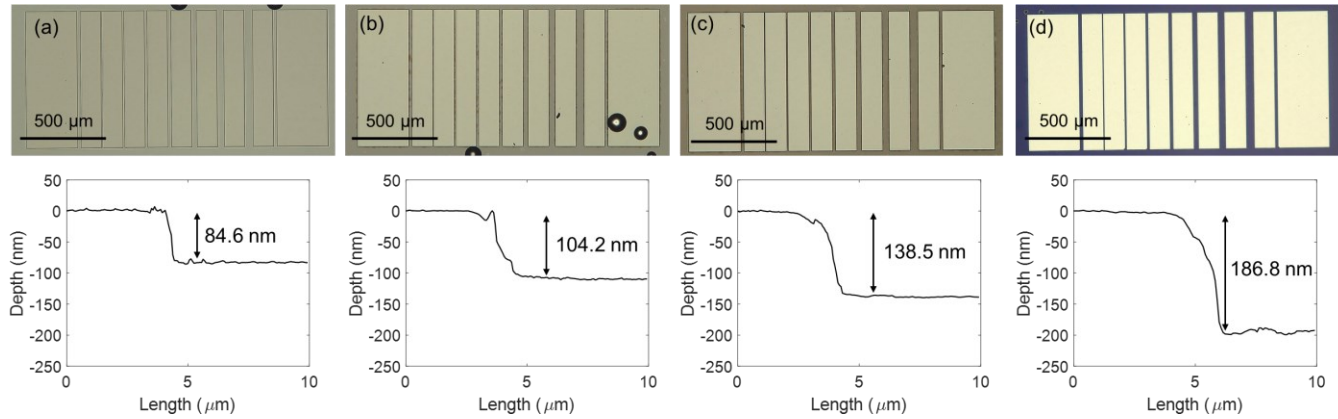## 6. Top view images of modified transmission line method devices and atomic force microscopy results

Figure S4. Top view images of modified transmission line method (M-TLM) devices with different etched depth and corresponding depth profiling results using atomic force microscopy, which measures the depth from top surface of platinum metal pattern to SL-PCM surface. (a) The device without SL-PCM etched, where the depth corresponds just to the Pt thickness, (b) with SL-PCM etched for 30 seconds, (c) with SL-PCM etched for 40 seconds, and (d) with SL-PCM fully etched, where the ~110 nm thick thermally grown SiO_2 is exposed (see cross-section in main text Figure 3b).

Material	Electrical resistivity		References
	In-plane (Ω cm)	Cross-plane (Ω cm)	
Sb_2Te_3/GeTe SL	5.8×10^{-4}	1.1	This work
Sb_2Te_3/GeTe SL	4.8×10^{-3}	19.4	Ref 20.
In_2Se_3 nanowire SL	2×10^{-3}	40	Ref 21.
Sb_2Te_3	1×10^{-3}	4×10^{-3}	Ref 22.
Sb_2Te_3/GeTe SL	7.8×10^{-4}	-	Ref 23.
Sb_2Te_3/GeTe SL	8.2×10^{-4}	-	Ref 24.
Sb_2Te_3/$Ge_2Sb_2Te_5$ SL	9.2×10^{-4}	-	Ref 24.
Sb_2Te_3/Bi_2Te_3 SL	7.7×10^{-4}	-	Ref 25.

Table S2. Reported data of electrical resistivities in the in-plane and cross-plane directions of different materials including the Sb_2Te_3/GeTe superlattice (SL) explored in this work. All materials are (poly)crystalline, although deposition conditions can vary between samples and between studies.

Supporting References

1. Cahill, D. G. Analysis of Heat Flow in Layered Structures for Time-Domain Thermoreflectance. *Rev. Sci. Instrum.* **2004**, *75* (12), 5119–5122.
2. Lee, J.; Bozorg-Grayeli, E.; Kim, S.; Asheghi, M.; Philip Wong, H. S.; Goodson, K. E. Phonon and Electron Transport through $Ge_2Sb_2Te_5$ Films and Interfaces Bounded by Metals. *Appl. Phys. Lett.* **2013**, *102* (19), 191911.
3. Maris, H.; Tanaka, Y. Phonon Group Velocity and Thermal Conduction in Superlattices. *Phys. Rev. B.* **1999**, *60* (4), 2627–2630.

4. Bies, W. E.; Radtke, R. J.; Ehrenreich, H. Phonon Dispersion Effects and the Thermal Conductivity Reduction in GaAs/AlAs Superlattices. *J. Appl. Phys.* **2000**, *88* (3), 1498–1503.

5. Chen, G. Size and Interface Effects on Thermal Conductivity of Superlattices and Periodic Thin-Film Structures. *J. Heat Transfer* **1997**, *119* (2), 220–229.

6. Wang, Y.; Liebig, C.; Xu, X.; Venkatasubramanian, R. Acoustic Phonon Scattering in Bi_2Te_3/Sb_2Te_3 Superlattices. *Appl. Phys. Lett.* **2010**, *97* (8), 083103.

7. Barsoum, M. W.; Rawn, C. J.; El-Raghy, T.; Procopio, A. T.; Porter, W. D.; Wang, H.; Hubbard, C. R. Thermal Properties of Ti_4AlN_3. *J. Appl. Phys.* **2000**, *87* (12), 8407–8414.

8. Battaglia, J. L.; Kusiak, A.; Schick, V.; Cappella, A.; Wiemer, C.; Longo, M.; Varesi, E. Thermal Characterization of the SiO_2-$Ge_2Sb_2Te_5$ Interface from Room Temperature up to 400 °C. *J. Appl. Phys.* **2010**, *107* (4), 044314.

9. Dutta, P.; Bhoi, D.; Midya, A.; Khan, N.; Mandal, P.; Shanmukharao Samatham, S.; Ganesan, V. Anomalous Thermal Expansion of Sb_2Te_3 Topological Insulator. *Appl. Phys. Lett.* **2012**, *100* (25), 251912.

10. Shaltaf, R.; Gonze, X.; Cardona, M.; Kremer, R. K.; Siegle, G. Lattice Dynamics and Specific Heat of α-GeTe: Theoretical and Experimental Study. *Phys. Rev. B.* **2009**, *79* (7), 075204.

11. Meng, W. J.; Eesley, G. L. Growth and Mechanical Anisotropy of TiN Thin Films. *Thin Solid Films* **1995**, *271* (1–2), 108–116.

12. Lyeo, H. K.; Cahill, D. G.; Lee, B. S.; Abelson, J. R.; Kwon, M. H.; Kim, K. B.; Bishop, S. G.; Cheong, B. K. Thermal Conductivity of Phase-Change Material $Ge_2Sb_2Te_5$. *Appl. Phys. Lett.* **2006**, *89* (15), 151904.

13. Yang, F.; Ikeda, T.; Snyder, G. J.; Dames, C. Effective Thermal Conductivity of Polycrystalline Materials with Randomly Oriented Superlattice Grains. *J. Appl. Phys.* **2010**, *108* (3), 034310.

14. Askarpour, V.; Maassen, J. Unusual Thermoelectric Transport Anisotropy in Quasi-Two-Dimensional Rhombohedral GeTe. *Phys. Rev. B* **2019**, *100* (7), 75201.

15. Campi, D.; Paulatto, L.; Fugallo, G.; Mauri, F.; Bernasconi, M. First-Principles Calculation of Lattice Thermal Conductivity in Crystalline Phase Change Materials: GeTe, Sb_2Te_3, and $Ge_2Sb_2Te_5$. *Phys. Rev. B* **2017**, *95* (2), 024311.

16. Cahill, D. G.; Watson, S. K.; Pohl, R. O. Lower Limit to the Thermal Conductivity of Disordered Crystals. Phys. Rev. B **1992**, 46 (10), 6131–6140.

17. Venkatasubramanian, R.; Siivola, E.; Colpitts, T.; O'Quinn, B. Thin-Film Thermoelectric Devices with High Room-Temperature Figures of Merit. *Nature* **2001**, *413* (6856), 597–602.

18. Simkin, M. V.; Mahan, G. D. Minimum Thermal Conductivity of Superlattices. *Phys. Rev. Lett.* **2000**, *84* (5), 927–930.

19. Yang, B.; Chen, G. Partially Coherent Phonon Heat Conduction in Superlattices. *Phys. Rev. B.* **2003**, *67* (19), 195311.

20. Yang, Z.; Xu, M.; Cheng, X.; Tong, H.; Miao, X. Manipulation of Dangling Bonds of Interfacial States Coupled in GeTe-Rich GeTe/Sb_2Te_3 Superlattices. *Sci. Rep.* **2017**, *7* (1), 17353.

21. Peng, H.; Xie, C.; Schoen, D. T.; Cui, Y. Large Anisotropy of Electrical Properties in Layer-Structured In_2Se_3 Nanowires. *Nano Lett.* **2008**, *8* (5), 1511–1516.

22. Hinsche, N. F.; Yavorsky, B. Y.; Mertig, I.; Zahn, P. Influence of Strain on Anisotropic Thermoelectric Transport in Bi_2Te_3 and Sb_2Te_3. Phys. Rev. B - Condens. Matter Mater. Phys. **2011**, 84 (16), 165214.

23. Tominaga, J.; Kolobov, A. V.; Fons, P. J.; Wang, X.; Saito, Y.; Nakano, T.; Hase, M.; Murakami, S.; Herfort, J.; Takagaki, Y. Giant Multiferroic Effects in Topological GeTe-Sb_2Te_3 Superlattices. *Sci. Technol. Adv. Mater.* **2015**, *16* (1), 14402.

24. Cecchi, S.; Zallo, E.; Momand, J.; Wang, R.; Kooi, B. J.; Verheijen, M. A.; Calarco, R. Improved Structural and Electrical Properties in Native Sb_2Te_3/$Ge_xSb_2Te_{3+x}$ van Der Waals Superlattices Due to Intermixing Mitigation. *APL Mater.* **2017**, *5* (2), 026107.

25. Hinsche, N. F.; Yavorsky, B. Y.; Gradhand, M.; Czerner, M.; Winkler, M.; König, J.; Böttner, H.; Mertig, I.; Zahn, P. Thermoelectric Transport in Bi_2Te_3/Sb_2Te_3 Superlattices. *Phys. Rev. B* **2012**, *86* (8), 085323.